

The Development and Hover Test Application of a Projection Moiré Interferometry Blade Displacement Measurement System

Martin K. Sekula
martin.k.sekula@nasa.gov
NASA Langley Research Center
Hampton, Virginia

Abstract

Projection moiré interferometry (PMI) was employed to measure blade deflections during a hover test of a generic model-scale rotor in the NASA Langley 14x22 subsonic wind tunnel's hover facility. PMI was one of several optical measurement techniques tasked to acquire deflection and flow visualization data for a rotor at several distinct heights above a ground plane. Two of the main objectives of this test were to demonstrate that multiple optical measurement techniques can be used simultaneously to acquire data and to identify and address deficiencies in the techniques. Several PMI-specific technical challenges needed to be addressed during the test and in post-processing of the data. These challenges included developing an efficient and accurate calibration method for an extremely large (65 inch) height range; automating the analysis of the large amount of data acquired during the test; and developing a method to determinate the absolute displacement of rotor blades without a required "anchor point" measurement. The results indicate that the use of a single-camera/single-projector approach for the large height range reduced the accuracy of the PMI system compared to PMI systems designed for smaller height ranges. The lack of the "anchor point" measurement (due to a technical issue with one of the other measurement techniques) limited the ability of the PMI system to correctly measure blade displacements to only one of the three rotor heights tested. The new calibration technique reduced the data required by 80 percent while new post-processing algorithms successfully automated the process of locating rotor blades in images, determining the blade quarter chord location, and calculating the blade root and blade tip heights above the ground plane.

Background

A hover test of a generic model-scale rotor was conducted in the NASA Langley 14x22 subsonic wind tunnel's hover facility. One of the primary goals of this test was to demonstrate and assess the capability to simultaneously acquire blade and wake measurements using several optical measurement techniques in preparation for a future wind tunnel test. These optical measurement techniques included pressure sensitive paint (PSP), oil flow visualization, particle image velocimetry (PIV), photogrammetry, and projection moiré interferometry (PMI). The focus of this paper is on the development and application of PMI during this test.

PMI is a non-contact optical measurement technique which employs a light source projecting a line pattern on a test article to facilitate the calculation of its surface deformation¹⁻⁴. The strength of PMI, compared to other optical displacement measurement techniques is that it can provide continuous out-of-plane blade displacement measurements instead of discrete measurements at a limited number of locations. This technique has been previously utilized for rotorcraft applications^{1,2}. Rotorcraft-specific PMI was first demonstrated during

the Rotor Wake/Configuration Aerodynamic Test in the NASA Langley 14x22 subsonic wind tunnel. Since that test, PMI has been successfully applied to determine blade deflections during a wind tunnel test of the Active Twist Rotor in the NASA Langley Transonic Dynamics Tunnel. The acquired PMI data provided flap-wise blade bending measurements and collaborated other data measuring the amplitude, frequency, and phase of active blade deformations.

Test Overview

The rotor tested is a generic, model-scale 4-bladed articulated rotor installed on a sting-mounted testbed called the General Rotor Model System (GRMS). The general properties of this rotor are provided in Table 1. A planform view of the rotor blade is provided in Figure 1. Further information on this rotor can be found in Reference 5.

Table 1. Rotor properties.

Property	Value
Rotor radius (in)	66.5
Blade chord (in)	5.45
Number of blades	4
Tip speed (ft/s)	666
Linear blade twist (deg)	-14
Rotor solidity	0.1033
Flap hinge station (in)	3
Lag hinge station (in)	3

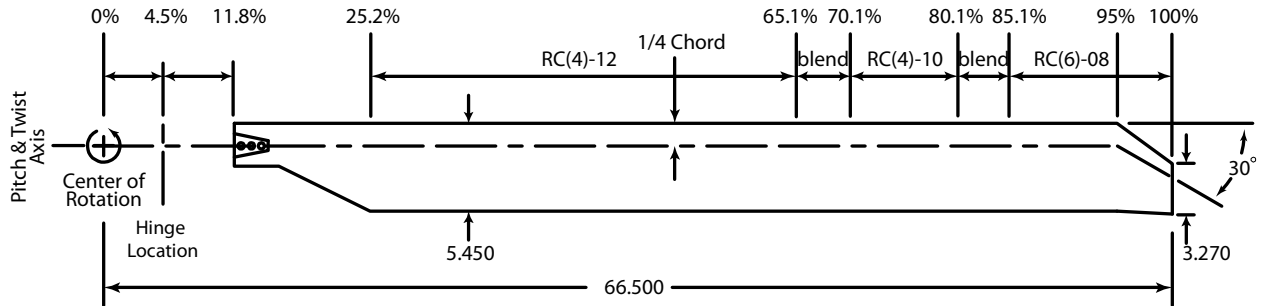


Figure 1. Rotor planform (in).

Figure 2 presents an image of the GRMS undergoing hover testing. In this figure, three of the optical measurement techniques can be discerned: illuminated PIV particles in the lower right corner, blue photogrammetry targets on the fuselage, and a PMI line pattern projected onto the lower surface of the rotor blades and fuselage. Since the various optical measurement techniques rely on illuminating the test article, the frequency of the light source for each system was selected to minimize interference with the other measurements and the cameras for these systems were equipped with proper optical filters.

Data were acquired for a hovering rotor at three heights (h) above a ground plane, $0.55D$, $0.75D$, and $0.90D$, where D is the rotor diameter. At each height, the rotor was trimmed to three thrust coefficients (C_T), 0.004 , 0.006 , and 0.008 . The primary data for all the optical techniques were acquired at the 270 degree rotor

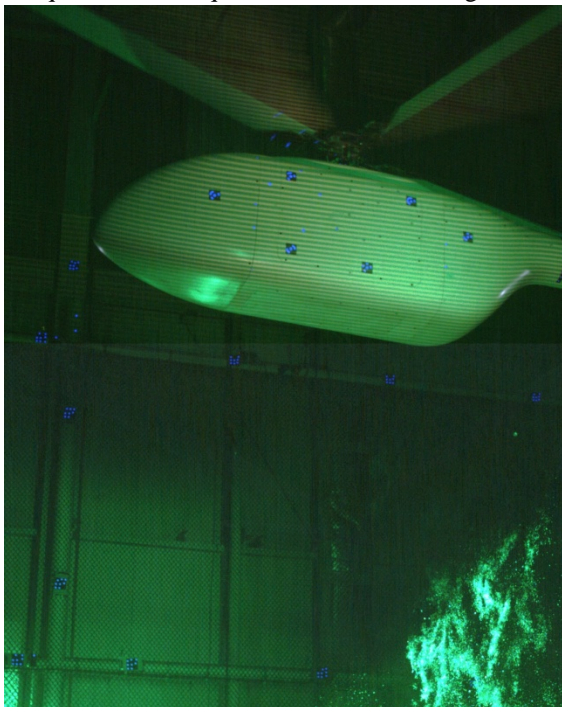


Figure 2. GRMS undergoing hover testing.

azimuth. For some conditions, PMI measurements were also acquired at other azimuth angles ranging from 255 to 285 degrees, although this paper will focus on the primary data. For each PMI data point, up to 100 images were acquired. During the course of the three day test, approximately $10,000$ images were recorded. The large number of images acquired and the large range of rotor heights examined required new techniques to be developed to calibrate the system and analyze the data in an efficient manner.

Equipment Setup

Figure 3 provides a schematic of the PMI equipment and outlines their interconnectivity. The basic PMI system consisted of a charge-coupled-device camera sensitive in the near infrared range, a 795 nanometer Coherent™ Fiber Array Package laser connected via an armored fiberoptic cable to a custom-built projector, and a computer with a frame grabber board to save the images acquired by the camera. Additional equipment included a NASA Langley-developed Rotor Azimuth Synchronization Program (RASP) module to synchronize image acquisition and laser illumination with the rotor azimuth, and a signal generator to transform RASP signals into transistor-transistor logic

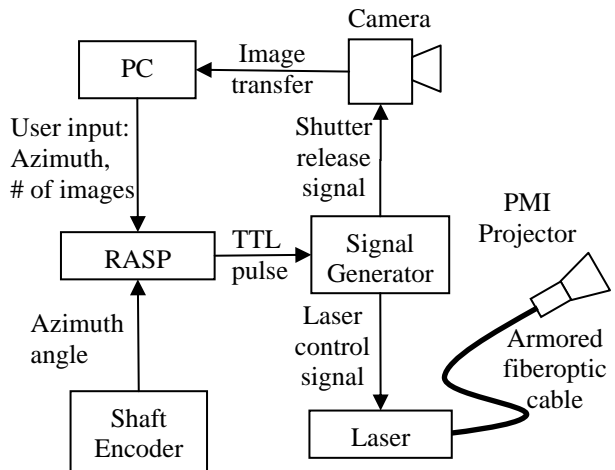


Figure 3. PMI equipment setup and information flow diagram.

(TTL) signals controlling the camera and the laser. The TTL outputs from the signal generator controlled the shutter release and shutter speed on the camera, as well as the duration of the laser pulse and its timing with respect to the camera shutter release.

The projector was a custom three-optical component assembly presented in Figure 4a, with a disassembled view provided in Figure 4b. The optics are held in an adjustable optical mount (elements labeled “1” in the figure), with the optics arranged such that laser light is first passed through a collimating lens (2) to align the beam, then a Ronchi ruling (3) to produce the line pattern, and finally a camera lens (4) to project and focus the line pattern on the test article.

Calibration

The assembled PMI calibration rig is presented in Figure 5. The calibration rig consisted of a frame supporting an adjustable height flat plate and a laser distance meter to measure the height of the plate above the ground plane. The rotor heights investigated during this test required that the PMI system be calibrated for heights ranging from 65 to 130 inches above the ground plane. A new calibration procedure was developed to accommodate this extremely large calibration range. The procedure had to address two significant technical challenges: system nonlinearity and the sheer volume of data required for calibration.

The first challenge, system nonlinearity, arises from the fact that the required calibration range is considerably larger than the range of heights within which system linearity can be assumed. The nonlinearity inherent to the PMI measurement method is demonstrated in Figure



Figure 4. Projector assembly.

6a where the average height of the calibration plate in the lateral direction is presented as a function of the longitudinal location on the calibration plate. In this figure, the entire 65 inch height range was characterized using a single linear calibration. Each line in Figure 5 represents the PMI-measured height of the calibration plate based on images acquired throughout the calibration process. The impact of the linear assumption for the PMI system manifests itself at the extrema of the heights examined. At larger heights, the PMI data incorrectly suggests that the calibration plate is tilted instead of horizontal, while at lower heights the calibration plate appears to be bent.

There are two main contributors to the PMI system nonlinearity. The first contributor is the use of non-telecentric optics in both the camera and projector. The second is the effect of perspective on the projected line pattern which becomes dominant below a certain height. As the calibration plate moves towards the camera (decreasing height), the oblique projection of the line pattern onto the calibration plate increases the line thickness and spacing. Significant changes in the projected line thickness and spacing can alter the characteristics of the moiré fringe pattern produced by interfering the acquired calibration plate images with a reference image. A substantial change in the fringe pattern can result in inaccurate displacement measurements, such as the ones visible below 85 inches on the left hand side in Figure 6a. To avoid this problem, the required range of heights was divided into ten overlapping segments, each individually calibrated.

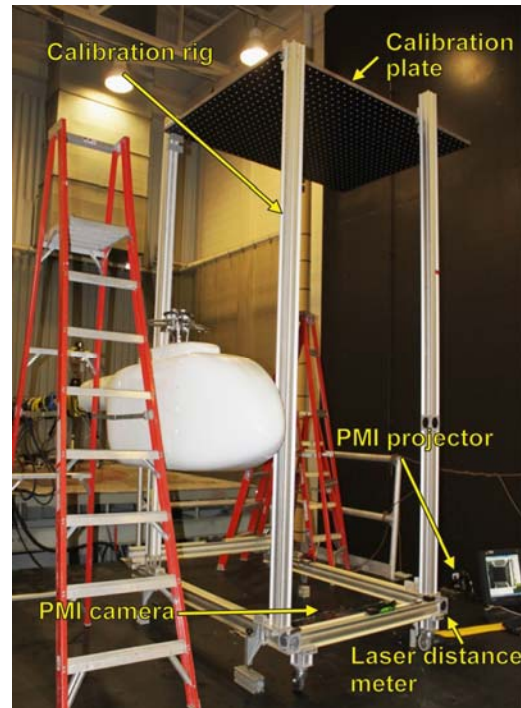
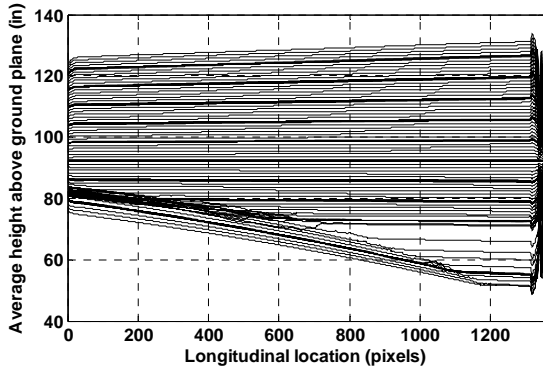
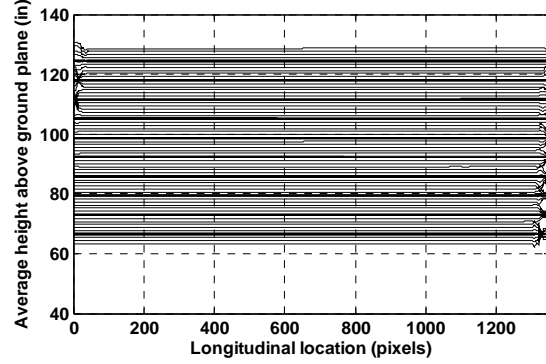


Figure 5. PMI calibration equipment.



(a) One calibration range



(b) Ten calibration ranges

Figure 6. PMI-determined calibration plate height determined from calibration images.

By reducing the height range for each calibration, the PMI system can once again be treated as a linear system within each height range. The PMI-derived calibration plate height determined using this ten-segment approach is provided in Figure 6b. Except for some error at the image edges caused by low-pass filters employed in the phase extraction process, the PMI system measures the correct height and horizontal orientation of the calibration plate.

The second technical challenge was minimizing the effort and the amount of data required to calibrate the PMI system. The calibration process determines the rate of change of the interference phase as a function of height for every pixel in the PMI image. The interference phase is a discontinuous function with respect to height that is limited to a $-\pi$ to $+\pi$ radians range. A sample interference phase function for a single image pixel is presented in Figure 7 (wrapped phase, conventional method). As the phase reaches either of the $\pm\pi$ limits it becomes discontinuous, resulting in a saw tooth-like waveform. The distance that an object must be moved for the phase to change by 2π radians is defined as the fringe contour interval (FCI). A graphical representation of FCI can also be found in Figure 7.

In a conventional calibration method, calibration plate images must be acquired at a minimum of four heights within each FCI. (An estimate for the FCI can be obtained based on the relative position of the camera and projector with respect to the calibration plate and the projected line spacing on the plate.) Acquiring data at these height intervals makes it possible to identify the phase discontinuities and remove them by adjusting the phase by $2\pi n$ radians, where n is an integer. Once these discontinuities are removed (see Figure 7; unwrapped phase, conventional method), a linear function relating phase to displacement can be determined.

Calibrating the PMI system using the conventional method over the desired height range would require the acquisition of data at several hundred distinct heights. Acquiring such a large number of images would not only be labor intensive, but also time prohibitive. Therefore, a predictor-corrector (P-C) calibration method was developed which reduced the number of required images while maintaining calibration accuracy. This method requires that images be acquired at the center of the calibration range for a minimum of four heights at spacing intervals comparable to the conventional method. Remaining calibration images are acquired at significantly larger height intervals, 1 to 2 FCIs, across the entire calibration range. (See Figure 7; wrapped phase, P-C method.)

In the initial step, the four closely spaced images are processed, any phase discontinuities are eliminated, and a curve fit of the phase data is calculated. Next, the images at larger height intervals are processed. Starting with the image acquired at a height closest to the center of the calibration range, the curve fit is used to extrapolate the interference phase for that height. This extrapolated interference phase will not be exact due to measurement uncertainties in the curve fit data and the

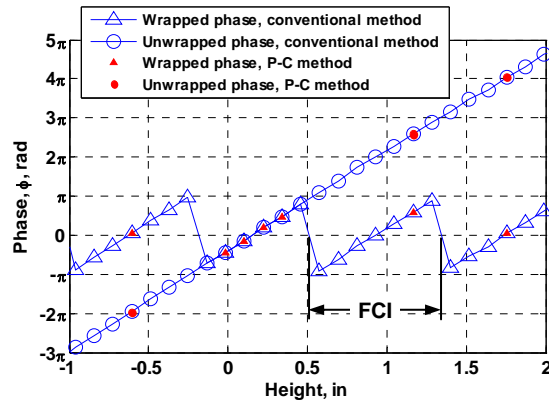


Figure 7. Wrapped and unwrapped phase data during calibration process.

forementioned nonlinearities inherent in the PMI analysis. The extrapolated phase must be corrected with the following equation:

$$\phi_c = \text{quotient}\left(\frac{\phi_e - \phi_m}{2\pi}\right)2\pi + \phi_m$$

Where ϕ_c is the corrected interference phase, ϕ_e is the extrapolated phase, ϕ_m is the measured phase, and *quotient()* is a function that rounds to the lower integer. Once the corrected phase is calculated, the curve fit is updated based on the additional data and the process is repeated for all the remaining calibration heights. (See Figure 7; unwrapped phase, P-C method.)

The ability of the predictor-corrector calibration method to accurately calibrate a PMI system was examined prior to the test. A PMI system calibration was conducted employing the same equipment with a camera-projector placement similar to the hover test. Data were acquired in 0.1 inch height intervals for the first two inches of the calibration range, followed by 1 inch intervals for the next 6 inches. Calibration coefficients for the PMI system were determined twice – first using the conventional method with data from the first 2 inches of the calibration range and then using the P-C method using six heights from the entire 8 inch range. Figure 8 presents a comparison of the RMS errors (PMI minus laser distance meter) determined for conventional and P-C calibration methods across the 8 inch height range. The P-C calibration method resulted in an RMS error of less than 0.03 inches across the entire range of heights, confirming the applicability of this approach. The conventional calibration method provided slightly better accuracy within the two inch range that it was calibrated for, but exhibited much larger errors outside that calibration range. This growth in error outside the calibration range indicates that the PMI system must be calibrated across the entire expected range of heights.

The predictor-corrector calibration method allows a PMI system calibration to be conducted with

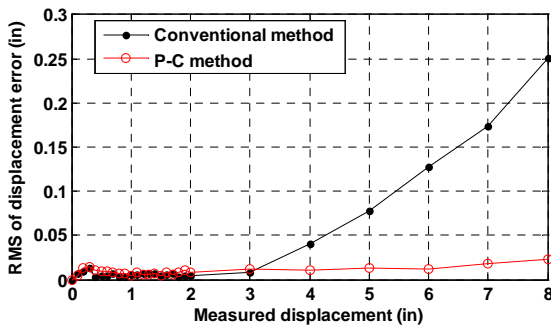


Figure 8. Comparison of RMS error for conventional and predictor-corrector calibration methods.

significantly fewer data points than the conventional calibration method. Using the conventional method, where the height increment is based on the minimum FCI length, approximately 650 sets of images would be necessary to calibrate the PMI system for the height range required for the hover test. Using the new P-C method, the PMI system was calibrated using 111 sets of images – more than an 80 percent reduction in the number of images required.

Analysis Techniques

During the three-day test, over 10,000 images were acquired for different rotor heights and thrust conditions. The analysis of this large quantity of data required a significant amount of automation to make the analysis process feasible and efficient. There are several steps in the postprocessing procedure for each image:

1. Removal of image distortion
2. Blade identification
3. Interference phase extraction
4. Displacement calculation
5. Extraction of pertinent data

A more detailed discussion of each of these steps is presented below.

Removal of image distortion

Perspective distortion and optical aberrations result in images of rotor blades that are stretched or warped. These distortions are eliminated through a software correction thereby providing an image more useful for analysis. To identify and characterize the distortions, an image is acquired of a flat plate with an equidistantly spaced dot pattern painted on it. An algorithm determines how the image must be stretched such that the dot pattern once again appears to be equidistant. This “stretching template” is then applied to all PMI images. A sample set of raw and dewarped images can be found in Reference 1 and algorithm details are available in Reference 6.

Blade identification

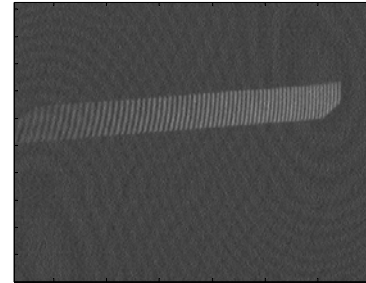
Sting flexibility produced image-to-image variability in the blade location precluding the use of a single image mask, a graphical representation of the location of an object in an image, to provide the location of a rotor blade for an entire set of images acquired at a specific flight condition. Therefore, a method was developed to automatically identify the location of rotor blades in the PMI images and to generate unique image masks for each image. Image masks improve postprocessing

efficiency by eliminating extraneous data from the phase unwrapping process. In the present analysis, image masks are also employed to identify and extract specific data about the rotor blades.

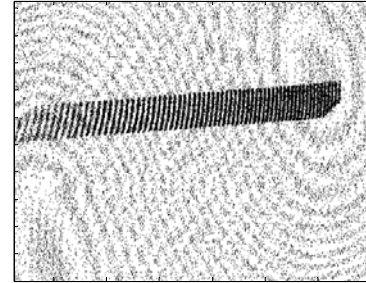
Since the hover test was conducted in a dark environment, a multi-step process based on light intensity and image contrast was developed to locate the blades and generate these image masks. A graphical representation of sample results for each step in this analysis is provided Figure 9. The starting point in the analysis, a dewarped image of the rotor blade, is presented in Figure 9a. It should be noted that the contrast in these images is extremely poor, where the background noise is of the same order of magnitude as the blade illumination intensity. The source of this low contrast was a combination of a large projection field and extremely short laser pulse duration and fast shutter speeds required to minimize image blur. In the first step of the mask generation process, the mean and the standard deviation values of the light intensity for the entire image are calculated and pixels whose intensity is greater than the sum of the mean and standard deviation values are identified (Figure 9b.)

The second step in the mask generation process is to eliminate background noise pixels that satisfied the light intensity criteria in step one. These pixels appear in the background of Figure 9b as a series of dark bands. The background noise rejection is accomplished by scanning the entire image with a moving window where the pixel at the center of this square window is either kept or rejected based on the number of high-light-intensity pixels within the window. The window size is set to 9x9 pixels, and the pixel at the center of the window is retained if at least 45 percent of the pixels in the window exceed the intensity threshold. The result of this windowing technique is presented in Figure 9c. A second pass is required to eliminate all the background noise (Figure 9d.)

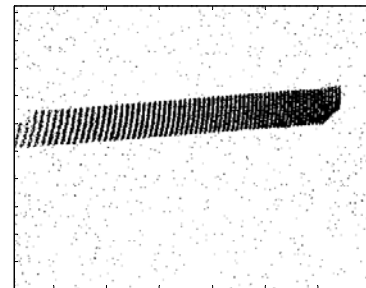
Since the PMI grid line projection results in a striped pattern of light intensity across the rotor blade target, only the illuminated segments of the rotor blade are highlighted in Figure 9d. Therefore the final step in the image mask generation process is to develop a solid outline of the blade by filling the areas between the segments. The algorithm developed to perform this task sequentially selects each highlighted pixel in Figure 9d and identifies any other highlighted pixels within a specified radius around it. For this application, the radius is set at 20 pixels. Any pixels located directly between the central and other identified pixels are themselves highlighted. Repeating this process for each highlighted pixel in the image results in the final image mask presented in Figure 9e.



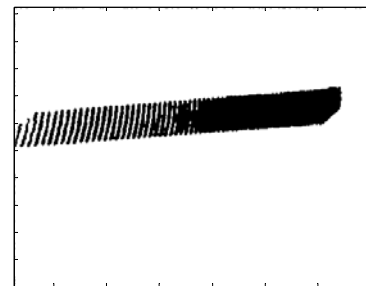
(a) Dewarped image



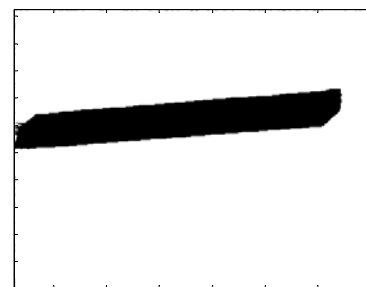
(b) Intensity-based pixel identification



(c) Windowing, first pass



(d) Windowing, second pass



(e) Final image mask

Figure 9. Steps in image mask generation.

Interference phase extraction

A critical element of the PMI analysis is the interference phase extraction. The phase extraction is achieved using a 4-interferogram process outlined in Reference 1. The interferograms are produced by superimposing acquired images with a set of computer-generated reference grid patterns. Typical superimposition techniques include addition, subtraction, and multiplication⁷. For this application, multiplicative superposition is employed due to its common usage and the strong moiré fringe patterns it produces^{7,8}.

The computer-generated reference grid pattern used to produce the interferograms should be similar to the projected grid pattern, therefore a calibration image, such as the one presented in Figure 10, is used as a template to create the reference grids. Typically, a Fast Fourier Transform (FFT) is employed to determine the dominant frequency of the line pattern across the image and produce these reference grids. These FFT-developed grids will consist of a constant wavelength grid pattern, but as noted in Figure 10, the wavelength changes across the calibration image due to the oblique placement of the projector with respect to the target. Interferograms created by interfering a constant wavelength reference grid with an image of a varying wavelength grid can produce a highly nonlinear interference phase function across the image that may complicate the calibration process. Therefore an alternate approach based on instantaneous frequency was developed to generate the reference grid.

Employing an instantaneous frequency approach results in much less variable and more intuitive interference phase values across the image. In the present analysis, the instantaneous frequency is calculated using a Hilbert transform. Before a Hilbert transform is applied, some additional data manipulation is required to remove the mean and normalize the amplitude of the light intensity of the calibration image⁹. A comparison of the waveforms of the computer-generated grid and the light

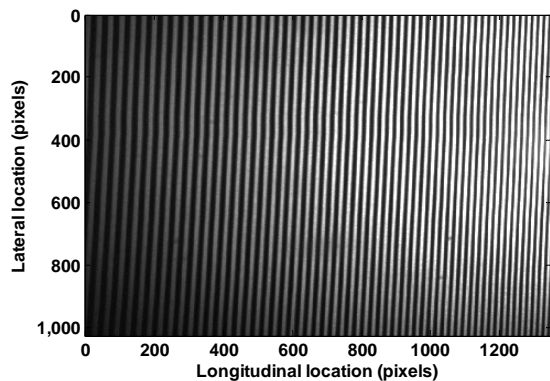


Figure 10. Calibration image.

intensity for the center row from Figure 10 is presented in Figure 11. The computer-generated grid properly matches the change in wavelength of the projected line pattern, although minor discrepancies are visible at the edges of the image.

Once the interference phase is extracted, an algorithm employing the Goldstein branch cut method¹⁰ unwraps the phase (removes phase discontinuities) to create a continuous phase function across the image.

Displacement calculation

An inherent challenge with the PMI technique is that the determination of an absolute distance to the test article from the camera cannot be based on the measured interference phase alone. The cyclic nature of phase-based measurements, whereby computed phase values range from $-\pi$ to $+\pi$ radians, results in an ambiguity of the absolute distance between the camera and the test article. The general relationship between object distance, H , and interference phase is $H \sim 2\pi n + \phi$ where n is the integer number of interference fringes between the camera and test article and ϕ is the remaining fractional interference fringe phase. PMI measures ϕ , and the $2\pi n$ is indeterminate without some other measurement to indicate the absolute distance of at least one point on the test article from which the value of n can be determined.

The GRMS testbed was mounted on a flexible sting, therefore testbed kinematics could not be employed to determine the absolute distance from the ground plane to the root of the blade. As a result, it was decided that photogrammetry, an optical technique capable of locating a target in a 3-dimensional space, would be employed to provide the necessary additional measurement. Multiple targets were affixed to the blades and the acquisition of photogrammetry data was synchronized with the PMI acquisition through the RASP module in order to determine the absolute distance from the ground plane to the blade for each image.

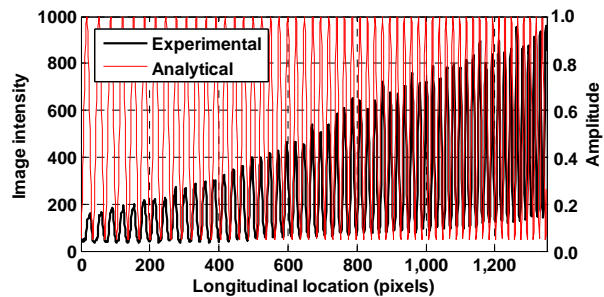


Figure 11. Comparison of projected line pattern to generated line pattern.

The post-test analysis of the photogrammetry data revealed problems precluding its use for determining the number of interference fringes, n . Therefore an alternative, non-displacement based technique was developed to determine the value of n . This new technique exploits a previously discussed feature of the PMI images – the changing wavelength of the projected grid pattern across an image. The spacing of the lines in the projected grid is proportional to the values of the calibration coefficients which relate the interference phase to displacements. Since the PMI calibration coefficients change across the image, an incremental change to the interference phase of the entire image not only changes the apparent object height, as determined by the PMI analysis, but also appears to rotate the object. This coupling of height and rotation can be employed to determine blade height based on the blade flapping angle measured by a potentiometer installed on the flap hinge. The implementation of this technique is outlined below:

Step 1. Locate the quarter chord of the blade in the PMI image. The quarter chord location is determined from blade leading and trailing edge locations based on the image mask border. Linear curve fits along the mask border are used to establish the actual location of the leading and trailing edges. Since blades, and therefore their image masks, feature a tapered root and a swept-tapered tip, the leading and trailing edge curve fits must account for these blade features as well as other image artifacts that were not eliminated by the image mask generation process. The curve fit process eliminates mask border pixels whose distance from the curve fit exceeds the standard deviation between the curve fit and the mask border.

Step 2. Select a calibration plate image as a reference image. The calibration plate height for this image should be similar to the nominal rotor height. Using this image, the fractional interference phase between the blade and a horizontal reference surface can be determined, and the known height of the calibration plate provides an initial estimate of the total interference phase.

Step 3. The interference phase calculated in step 2 is used to calculate an initial guess for the displacement of the rotor blade. A second order curve fit of the blade height along the quarter chord is calculated, and an RMS error-based rejection criterion is applied to remove phase unwrapping and filtering artifacts from the curve fit process (see left edge of Figure 12 for an example of a filtering artifact).

Step 4. The third step is repeated as the interference phase is changed in 2π radian intervals. For each new

blade displacement the blade flapping angle is calculated from the derivative of the quarter chord curve fit. The correct phase offset is determined by most closely matching the PMI-calculated blade root flapping angle with the measured blade flapping angle.

A graphical representation of steps 3 and 4 is presented in Figure 12. The figure illustrates the effect of the incremental change in interference phase on blade height. The red lines are PMI-calculated blade heights along the quarter chord for each 2π radians phase change and the dotted lines are quadratic curve fits of these blade heights. To the right of the figure are the calculated blade root flapping angles corresponding to each calculated blade height. The closest blade flapping angle in this data set to the mean of the measured blade flapping angle is highlighted in green. Using this technique, the PMI-based blade flapping angle was determined to be 2.36 degrees compared to a 2.41 degree measured value.

For each test condition, every image in a data set is processed using the technique outlined above. A sample distribution of quarter chord deflections calculated for a set of PMI images for a single data set is provided in Figure 13. The figure presents the PMI-derived quarter chord deflections in red and their curve fits in black. The abscissa denotes the distance from the

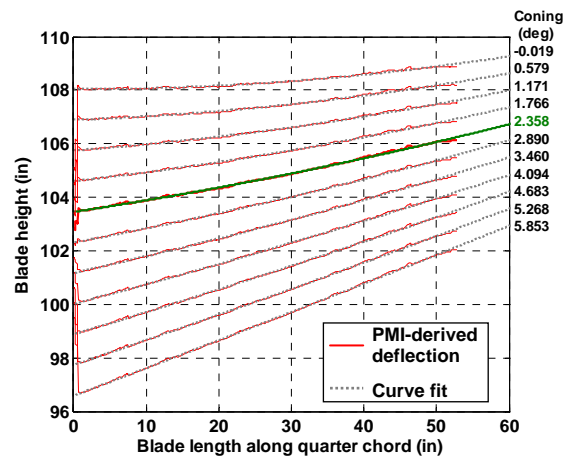


Figure 12. Sample blade height identification based on blade root flapping.

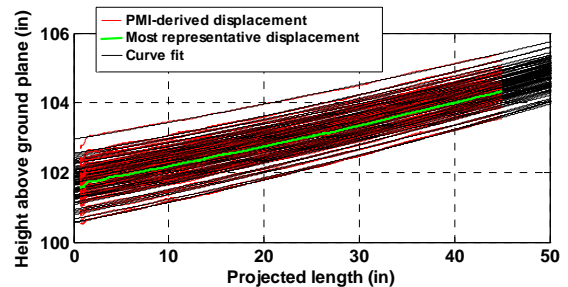


Figure 13. Distribution of blade heights.

edge of the image along the quarter chord axis projected onto the ground plane. The considerable amount of scatter in the blade displacements visible in this figure is a combined result of the significant dynamics experienced by the GRMS testbed, and uncertainty inherent to the flapping angle matching technique.

Figure 14 presents histograms for the measured blade flapping angle and the PMI-derived blade flapping angle, blade root height, and blade tip height corresponding to the blade deflections in Figure 13. The on-blade measured blade flapping angle histogram is based on data from 256 rotor revolutions while the PMI data is based on 100 images (one per revolution). The PMI-derived flapping angle is an “instantaneous” measurement but it is determined by adjusting the interference phase to match an average flapping angle, not a flapping angle measured at the same instant that the image was acquired. This lack of time correlation between the two measurement techniques introduces a level of uncertainty in the blade displacement measurements and is a potential source of error in the PMI-determined deflections.

The data presented in these histograms are representative of the data acquired throughout the hover test. The measured blade flapping angle histogram appears to exhibit a Gaussian distribution, revealing a 0.5 degree scatter in measured data (see Figure 14a.) The PMI-determined blade flapping angle and blade root height histograms, Figures 14(b-d), do not exhibit a Gaussian distribution. This difference in distribution may be due to the limited number of images acquired (100 images versus 256 samples), although the mean and standard deviation values of the blade flapping angle, represented by black and red dashed lines respectively, agree reasonably well for the PMI and measured data. For this particular data set, the blade root height distribution resulted in a mean blade root height of 101.23 inches with a 0.495 inch standard deviation. The mean blade tip height was determined to be 104.75 inches above the ground plane, with a

standard deviation of 0.379 inches – slightly smaller than the blade root height standard deviation.

Typically, the rotor blade images are averaged to minimize image blur and produce a single PMI image¹ which is then employed in the analysis. The lack of repeatability in the PMI images necessitated a different approach to determining a nominal blade deformation. Instead of a single averaged image, in this work the most representative image in the data set is presented. This image is selected by most closely matching the mean blade root height for that PMI data set. The quarter chord displacement for this most representative image is highlighted in green in Figure 13. The PMI-derived displacement of the lower surface of the rotor blade is presented in Figure 15a and the corresponding PMI image, highlighting the computer-identified blade quarter-chord and leading and trailing edges, is provided in Figure 15b. Throughout the rest of this paper, it should be assumed that statements about PMI-derived deflections imply that measurements of the lower surface of the blade are being discussed, unless otherwise noted.

Extraction of pertinent data

Along with image processing, phase extraction, and blade deflection determination, it was necessary to automate the data extraction process to facilitate the efficient analysis of the large quantity of data acquired during the hover test. Data pertinent to this test included blade location in the acquired images, blade quarter chord displacement, and blade tip and blade root displacements.

Processes to locate the blade and determine its quarter chord displacements were previously discussed. The blade root height is determined from the quarter chord height measurements. The root of the blade, including the flap hinge, is obstructed in the images by the fuselage, therefore the blade displacement along the quarter chord needs to be extrapolated to the flap hinge.

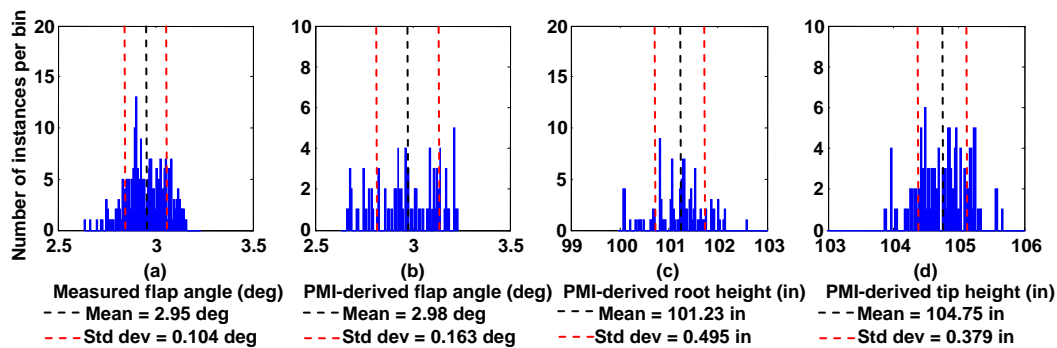
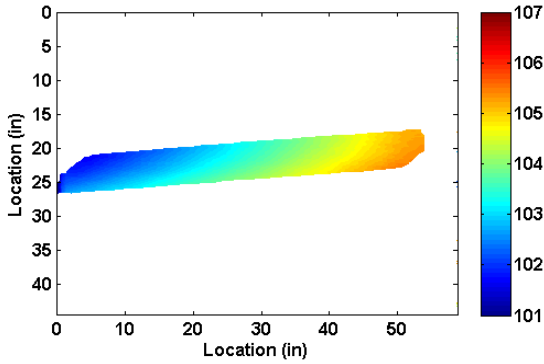
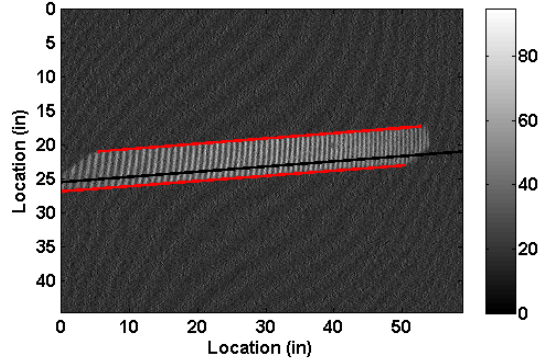


Figure 14. Histograms of the measured blade flapping angle and PMI-derived blade flapping angle, blade root height, and blade tip height.



(a) Height above the ground plane (in)



(b) Light intensity (out of 1024)

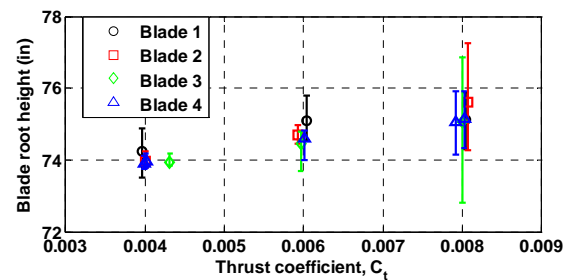
Figure 15. Sample blade height above ground plane and raw PMI image.

The previously calculated curve fit of the quarter chord height is used to determine the slope of the blade at the inboard edge of the image and to calculate the length of the blade visible in the image. The portion of the blade not visible in the image is assumed to be rigid, undergoing a rotation about the flap hinge. Based on these assumptions, the visible blade length, and the rotor radius, the flap hinge height (assumed to be the hub height) is determined.

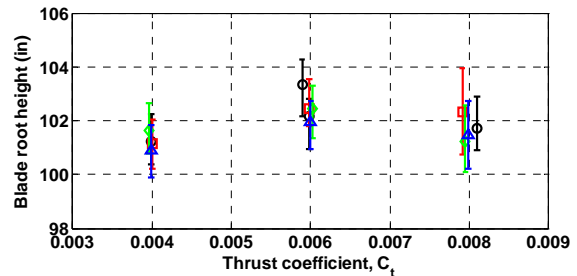
The blade tip height is calculated by averaging the height of a 5-by-5 pixel block centered at the quarter chord of the blade tip. The blade tip quarter chord location is identified by locating the quarter chord line in the swept-tapered portion of the rotor blade through a process akin to the one used to identify the blade quarter chord, but limited to the outer portion of the blade.

Results

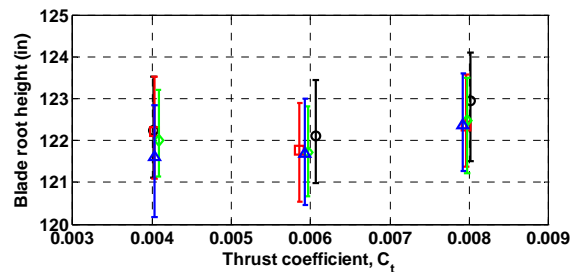
The blade root height above the ground plane as a function of rotor thrust for three nominal rotor heights of 0.55D, 0.75D and 0.90D is presented in Figure 16. At each thrust condition the hub height is calculated based on data acquired for each of the four blades. Error bars are included to provide the range of scatter in the PMI data. For a nominal rotor height of 0.55D, the hub height increases with increasing rotor thrust, indicating an increase in sting deflection with increasing load. For nominal rotor heights of 0.75D and 0.90D, the PMI-derived hub deflections are not proportional to the rotor thrust. This behavior points to a problem with the PMI data or postprocessing since the sting deflection, and therefore the rotor height, should increase with increasing thrust. The potential cause of this problem will be discussed in more detail in the “Data Quality” section of this paper. Since the PMI-derived deflections at rotor heights 0.75D and 0.90D were found to be not valid, only the 0.55D rotor height data will be discussed in further detail.



(a) $h = 0.55D$



(b) $h = 0.75D$



(c) $h = 0.90D$

Figure 16. Blade root height as a function of C_t .

The quarter-chord deflections as a function of radial station are presented in Figure 17 for the three thrust conditions investigated. These deflections do not include blade tip deflections along the local swept tip quarter chord line – they correspond to the overall blade quarter chord line depicted as a black line in Figure 15b. In this figure, several effects of rotor thrust on blade displacements can be identified. The most notable is the

effect of increasing rotor thrust on the overall blade height due to greater sting deflections. Other trends that can be discerned are the change in the blade flapping angle due to increasing rotor thrust and the elastic deformations of the blades, characterized by the curvature of the quarter chord deflection. The blade tip experiencing the highest thrust, $C_t = 0.008$, displays one of the potential problems with the PMI technique. Image blur and low contrast can result in phase discontinuities – locations on images where phase unwrapping algorithms fail. These discontinuities present themselves as irregularities of the blade surface. Another irregularity appearing at the blade root is an artifact of the low-pass filtering technique employed in the phase extraction that occurs at the edges of the images.

Quarter chord deflections for all four blades, including several repeat points, are presented in Figure 18. The low thrust condition, $C_t = 0.004$, provides the most repeatable blade displacements. As the rotor thrust is increased, Figure 18 indicates that the scatter in the blade displacements also grows. The probable cause for this increase in blade displacement scatter is a growth in fuselage dynamics as the model is excited by increasing inflow and other interactions arising from rotor operation in ground effect and flow recirculation within the hover facility.

A summary of the blade deflection data is presented in a tabular format in Table 2. At each nominal thrust condition, the measured blade flapping angle for blade 1 and the PMI-derived data for each rotor blade are presented. The PMI-derived data includes the mean and standard deviation values for the blade flapping angle, the hub height, and the blade tip height. The PMI-derived mean blade flapping angles agree well with the measured blade flapping angle values. It should be

noted that the PMI-derived blade flapping angles for all four rotor blades are determined by matching the blade flapping angle measured on blade 1 – a potential source of error if the blades are not tracked properly. In general, the table indicates a reasonable level of blade-to-blade repeatability for the PMI-derived blade deflections.

The continuous surface displacements corresponding to the quarter chord displacements presented in Figure 17 are provided in Figure 19. The phase discontinuities noted at the blade tip for the highest thrust condition, $C_t = 0.008$, are visible in Figure 19c. Likewise, some minor discontinuities are also visible at the blade edges in Figure 19b, $C_t = 0.006$. These discontinuities may be eliminated by improving grid line contrast in the PMI

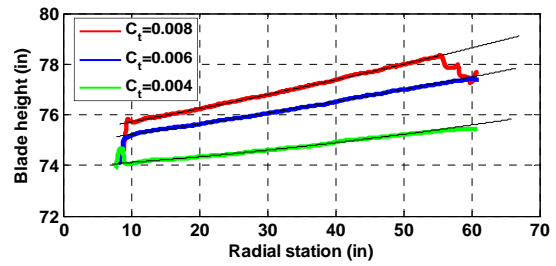


Figure 17. Quarter chord height as a function of C_t , $h = 0.55D$.

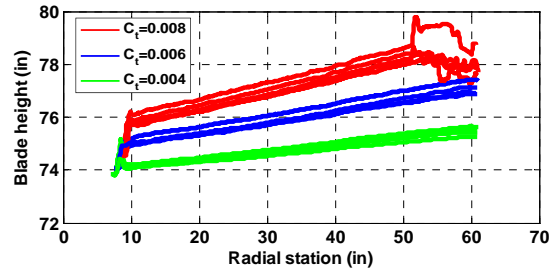


Figure 18. Quarter chord height repeatability (all four blades), $h = 0.55D$.

Table 2. Summary of blade measurements, $h = 0.55D$.

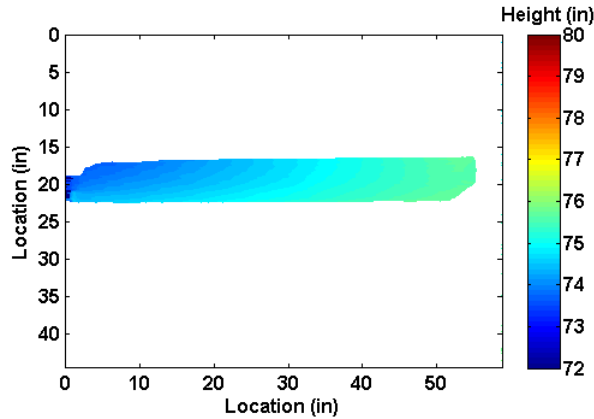
Nominal C_t	Blade number	Measured flap angle (deg)*	PMI-derived flap angle (deg)		PMI-derived hub height (in)		PMI-derived tip height (in)	
			Mean	Standard deviation	Mean	Standard deviation	Mean	Standard deviation
0.008	3	3.06	3.07	0.13	75.05	0.68	77.46 [†]	0.73 [†]
0.008	4	3.05	3.04	0.16	75.07	0.39	77.26 [†]	0.99 [†]
0.008	4	3.10	3.06	0.16	75.14	0.38	77.41 [†]	0.89 [†]
0.008	1	2.88	2.82	0.16	75.13	0.33	77.39 [†]	1.08 [†]
0.008	2	3.04	3.04	0.15	75.60	0.62	77.57 [†]	0.74 [†]
0.006	3	2.13	2.07	0.15	74.40	0.37	76.70	0.22
0.006	4	2.07	2.02	0.10	74.61	0.17	76.87	0.16
0.006	1	2.02	2.07	0.17	75.08	0.45	77.42	0.29
0.006	2	2.06	2.08	0.12	74.70	0.10	77.05	0.10
0.004	3	1.17	1.22	0.10	73.93	0.06	75.43	0.11
0.004	4	1.28	1.31	0.11	73.91	0.07	75.41	0.15
0.004	4	1.36	1.37	0.10	73.97	0.11	75.59	0.13
0.004	1	1.10	1.12	0.16	74.22	0.45	75.56	0.28
0.004	2	1.22	1.19	0.09	73.97	0.09	75.55	0.11

* Measurement acquired for blade 1.

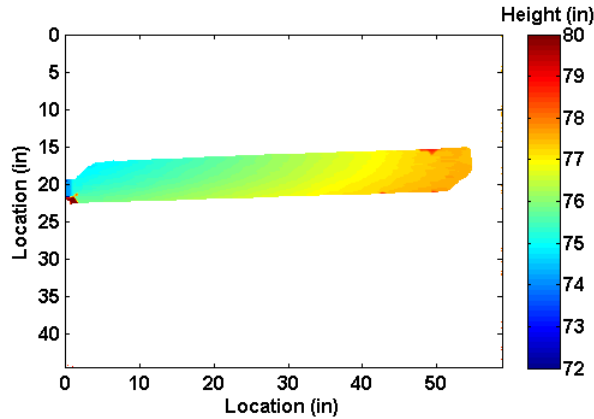
† Measurement affected by interference phase discontinuities.

images. In future tests, this contrast improvement could be accomplished by focusing the projector to illuminate a smaller area, or using a more powerful laser.

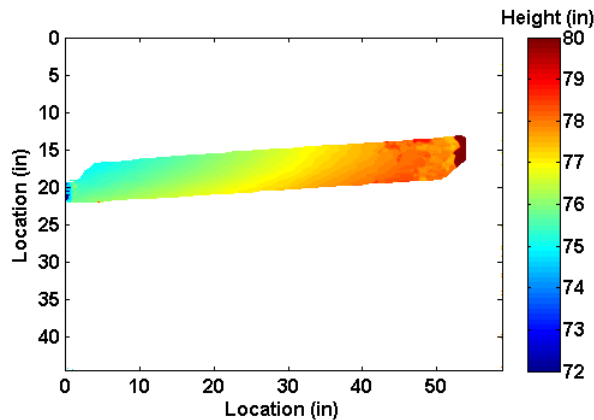
In Figures 19(a, b, and c) the rotor blades are oriented differently in each image, incorrectly giving the appearance that the images were acquired at different azimuth angles. This difference in blade orientation is



(a) $C_t = 0.004$



(b) $C_t = 0.006$



(c) $C_t = 0.008$

Figure 19. Blade displacement as a function of C_t , $h = 0.55D$.

caused by the change in the blade lag angle with increasing rotor thrust. The previously discussed capability to identify the location of the blade quarter chord in the images raised the possibility of using PMI images to determine the blade lag angle. Since the current data set lacked the information to determine the orientation of the 270 degree azimuth with respect to the image, only the relative blade lag angle between measurements at various thrust conditions is presented in Figure 20. Compared to the data obtained using a potentiometer attached to blade 1, the PMI image-determined change in blade lag angle as a function of rotor thrust is overpredicted. This overprediction may be caused by inadequacies in the algorithm creating the blade masks or an artifact of the image dewarping process. Both the potentiometer and image-based data indicate an exponential trend in the change in lag angle with increasing rotor thrust. Both techniques also indicate negligible changes in blade lag with varying rotor height. This technique requires further development, but it raises the possibility of providing a method for confirming blade lag angle measurements and blade-to-blade lag angle comparisons without the need for additional slipping channels to transfer data between the rotating and fixed frame.

Data Quality

There were several factors that influenced the quality of the PMI data acquired during this hover test. These factors can be loosely divided into two categories: ones that are inherent to the setup of the PMI system and problems arising from the blade flapping angle matching technique. This section will discuss these factors and potential solutions and improvements.

Image focus and grid line spacing

Among the major influences on the accuracy of the PMI data was the requirement to measure deflections over a large range of rotor heights. Satisfying this requirement with the available equipment while acquiring the

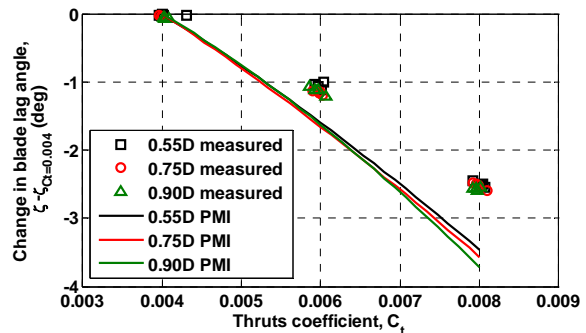


Figure 20. Mean change in blade lag angle as a function of C_t .

highest quality PMI images possible was a compromise weighing the effects of image field of view, image focus, projected grid focus, and projected grid spacing.

For the current PMI system setup, the image field of view increases as a function of rotor height. Both accuracy and resolution of the PMI system are dependent on the size of the field of view and their values can be approximated at 1/1500 and 1/2500 of the field of view¹. Figure 21 presents the RMS error calculated based on the PMI calibration plate images across the entire 65 inch range of heights. The calibration data suggests that under ideal conditions, measurement accuracy of the PMI system should be near 0.015 inches. A more realistic assessment based on the rule-of-thumb approximation provided in Reference 1 indicates an accuracy ranging from 0.05 to 0.1 inches, depending on the height of the rotor.

The sharpness of the image and the projected grid line pattern can also affect the PMI system accuracy. The camera and projector could not be refocused during the test to improve image quality for a specific rotor height, since any post-calibration adjustments would invalidate the calibration. Therefore the focus of both the camera and projector were adjusted before calibration to provide the best image and grid quality over the entire range of rotor heights.

PMI system sensitivity improves as the grid line spacing is reduced, but for practical considerations, a minimum line-to-line spacing of 5 pixels must be maintained¹. For the present test, the effects of rotor height on the grid line spacing needed to be considered. The non-telecentric nature of the projector optics results in wider grid spacing with increasing distance to the projector. At the same time, as the target moves further from the camera, each pixel on an image represents a larger area, thereby decreasing the image resolution. The location of the projector off to the side of the rotor also effects the grid line spacing. Decreasing the rotor height stretches the grid pattern across the image due to perspective. This perspective effect produces a wider grid line spacing at the blade root than at the blade tip and becomes more pronounced as the rotor height decreases.

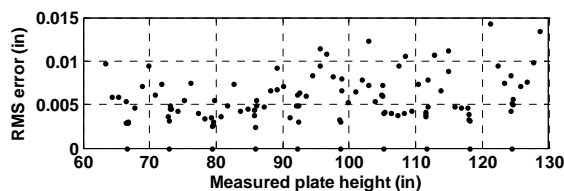
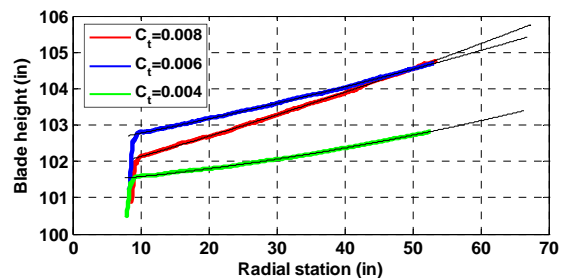


Figure 21. RMS error based on calibration plate measurement.

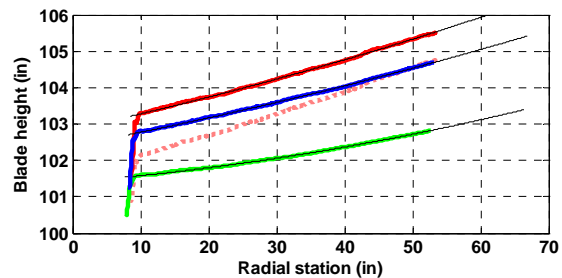
These field of view, focus, and grid spacing problems were examined using a mock-up prior to the test to identify the best choice of camera and projector lenses and Ronchi ruling line pitch. Even though a combination of lenses and ruling were found to satisfy the basic PMI requirements, system accuracy and sensitivity were compromised. In future tests, PMI system accuracy and sensitivity will be improved by employing multiple cameras and projectors to span the entire range of rotor heights, or limiting the range of rotor heights that the system is employed to measure.

Blade flapping angle matching

The blade flapping angle matching technique did not correctly determine blade displacements at rotor heights of 0.75D and 0.90D (see Figure 16 and discussion in the “Results” section.) Upon closer examination, it was determined that the blade flapping angle matching algorithm incorrectly determined the number of fringes between the ground plane and the rotor blade. This error is discernible in the quarter chord deflection data at a height of 0.75D, presented in Figure 22a. This figure incorrectly indicates that the overall blade height, and therefore sting elastic deflection, will be lower for a thrust condition of $C_t = 0.008$ than $C_t = 0.006$. By adjusting the $C_t = 0.008$ interference phase by 2π radians, Figure 22b, the resulting trends and range of blade root deflections are comparable to those determined for a nominal rotor height of 0.55D (compare Figures 22b and 17.) Although the exact cause of this problem has not been definitively identified, its likely source is a combination of changes



(a) Original phase



(b) Adjusted phase

Figure 22. Effect of interference phase adjustment on quarter chord blade deflection, $h = 0.75D$.

in the PMI calibration coefficients with increasing rotor height and uncertainty in the blade flapping angle measurement.

During the test, the large range of rotor heights examined required multiple calibrations, each for a different range of heights. For this PMI system configuration, as the calibration range moves away from the camera and projector, the calibration coefficients increase resulting in larger changes in displacements for every 2π radian increment. Simultaneously, the linear change of the coefficients across the image becomes more pronounced, creating a greater coupling between object height and rotation due to phase adjustments. This greater coupling results in larger changes in the PMI-derived blade flapping angle due to incremental changes in phase. This increase in the flapping angle increment is analogous to a reduction in the resolution of the data employed by the blade flapping angle matching technique which may affect the technique's accuracy.

Another contributor to the incorrect blade height is the lack of time correlation between the measured blade flapping angle and PMI image acquisition. A histogram of the measured blade flapping angle presented in Figure 14a illustrates a typical range of scatter in the data, indicating that the actual blade flapping angle at the time the image was acquired may be significantly different than the mean flapping angle that it is being matched to. This matching inaccuracy may be further compounded by the GRMS roll dynamics. PMI-derived blade flapping angle is measured with respect to the ground plane, not the rotor shaft. To explore the possible impact of GRMS roll on the blade flapping angle matching technique, a limited number of flight conditions were reexamined by adjusting the measured blade flapping angle to account for the instantaneous model roll angle. This limited exercise did not note any improvements in the blade deflection trends, but further work remains to completely rule out the impact of GRMS roll dynamics.

Ultimately, the blade flapping angle matching technique was developed as a work-around due unexpected problems with the photogrammetry data. This technique should not be relied on as a primary technique for determining the total interference phase due to the discussed shortcomings of this approach. Some potential improvements to the technique are: blade flapping angle data should be time-correlated with image acquisition; the range of heights to be measured with PMI should be reduced; and the height-rotation coupling should be optimized through improved camera and projector placement to provide better resolution for the flapping angle matching technique.

Conclusions

Projection moiré interferometry (PMI) was one of several optical measurement techniques used to acquire deflection and flow visualization data during a hover test in the NASA Langley 14x22 subsonic wind tunnel's hover facility. Some of the primary goals of the test were to demonstrate that multiple optical measurement techniques can be used simultaneously to acquire data for a generic model-scale rotor and to identify and address deficiencies in the techniques. PMI data were acquired for all four rotor blades for combinations of three rotor thrust coefficients ($C_t = 0.004, 0.006, \text{ and } 0.008$) and three rotor heights ($h = 0.55D, 0.75D \text{ and } 0.9D$).

The calibration of the PMI system and postprocessing of the large amount of data required new analysis techniques to be developed including:

- A methodology to calibrate a PMI system over an extremely large (65 inch) height range.
- A predictor-corrector calibration technique that reduced amount of data required for calibration.
- Automatic method to locate rotor blades in images.
- Automatic method to identify blade and blade tip quarter chord lines.
- Method to extrapolate an off-image rotor hub height based on blade displacements.
- A blade flapping angle-based technique to determine the total interference phase of the PMI measurement, in lieu of a conventional displacement measurement.

The results indicate that the use of a single camera and projector approach for the large height range reduced the accuracy of the PMI system. The blade flapping angle matching technique was partially successful at correctly determining the absolute blade height. The technique correctly determined the total interference phase for data at a nominal rotor height of $0.55D$. The new predictor-corrector calibration method reduced the calibration required data by more than 80 percent.

Acknowledgements

The author would like to thank Jim Meyers for providing the image dewarping software, Derry Mace for providing access to the test data, and Scott Bartram and Benny Lunsford for helping with the test setup and data acquisition. The author would also like to thank Gary Fleming for his insight and numerous discussions during the development of the analysis software.

References

1. Fleming, G. A. "Projection Moiré Interferometry for Rotorcraft Applications: Deformation Measurements of

- Active Twist Rotor Blades,” *Proceedings of the American Helicopter Society 58th Annual Forum*, Montreal, Canada, June 11-13, 2002.
2. Fleming, G. A. and Gorton, S. A. “Measurement of Rotorcraft Blade Deformation using Projection Moiré Interferometry,” *Journal of Shock and Vibration*, Vol. 7, No. 3, 2000.
 3. Yokozeki, S. and Mihara, S. “Moiré Interferometry,” *Applied Optics*, Vol. 18, No. 8, April 1979.
 4. Harding, K. G. and Harris, J. S. “Projection Moiré Interferometer for Vibration Analysis,” *Applied Optics*, Vol. 22, No. 6, March 1983.
 5. Wong, O. D., et al “Non-Intrusive Measurements of a Four-Bladed Rotor in Hover – A First Look,” *American Helicopter Society Aeromechanics Specialists’ Conference*, San Francisco, CA, January 20-22, 2010.
 6. Meyers, J. F. “Development of Doppler Global Velocimetry for Wind Tunnel Testing,” *AIAA 18th Aerospace Ground Testing Conference*, Paper 94-2582, Colorado Springs, CO, June 20-23, 1994.
 7. Bryngdahl, O. “Characteristics of superposed patterns in optics,” *Journal of the Optical Society of America*, 66, (1976), pp. 87-94.
 8. Lim, J. S., Kim, J., and Chung, M. S. “Additive Type Moiré with Computer Image Processing,” *Applied Optics*, Vol. 28, No. 13, July 1989, pp 2677-2680.
 9. Girolami, G. and Vakman, D. “Instantaneous frequency estimation and measurement: a quasi-local method,” *Measurement Science and Technology*, 13, June 2002, pp 909-917.
 10. Ghiglia, D. C. and Pritt, M. D. *Two-Dimensional Phase Unwrapping: Theory, Algorithms, and Software*, John Wiley & Sons, Inc. New York, 1998.